ROYAL SOCIETY
OF CHEMISTRY

COMMUNICATION

Check for updates

Significant decrease in the ionization energy of dinaphtho[2,3-b:2′,3′-f]thieno[3,2-b]thiophene (DNTT) solid induced by a pinacolborane group

Kazuo Takimiya, [iD] *[abc] Sayaka Usui,[b] Ryota Hanaki,[b] Kirill Bulgarevich, [iD] [a]
Kohsuke Kawabata, [iD] [ab] Kyohei Nakano [iD] [a] and Keisuke Tajima [iD] [a]

The low carrier density in organic semiconductors leads to high resistivity and contact resistance in electronic devices. Doping has been implemented to solve these issues. We describe herein a molecular modification approach to increase the carrier density. A representative p-type organic semiconductor, dinaphtho[2,3-b:2′,3′-f]thieno[3,2-b]thiophene (DNTT), was modified with a pinacolborane (Bpin) group, a reactive functional group in the Suzuki−Miyaura cross-coupling reaction. The resulting Bpin-modified DNTT (Bpin−DNTT) has a low-lying HOMO energy level at the single molecular level (5.4 eV below the vacuum level) and excellent transistor characteristics with mobility of greater than 2 cm^2 V^{-1} s^{-1}. However, the Bpin−DNTT solid was easily oxidized upon exposure to ambient air, generating hole carriers. To clarify this unprecedented behavior, we investigated Bpin−DNTT in detail through single-crystal field-effect transistor (SC-FET), electron spin resonance (ESR) spectroscopy, ultraviolet photoelectron spectroscopy (UPS), and theoretical calculations. The SC-FET and ESR spectra demonstrated that the surface of the Bpin−DNTT solid in air was readily oxidized, which was due to the significantly decreased ionization energy of 4.58 eV, confirmed by UPS. These results reveal the potential of the Bpin group to increase the carrier density in p-type organic semiconductors.

New concepts

So far, no functional group has been found that can induce a downward shift of the vacuum level (VL) in organic semiconductor solids, in contrast to fluorine groups that can induce an upward VL shift. The finding in this work is that the pinacolborane (Bpin) group, frequently used for Suzuki–Miyaura cross-coupling chemistry in organic synthesis, has an unprecedented function that induces a significant downward VL shift as well as an upward shift of the HOMO band edge of p-type organic semiconductor DNTT, resulting in a significant ionization energy decrease to 4.58 eV of Bpin–DNTT solid. As a result, the surface of the Bpin–DNTT molecule was easily oxidized by ambient air, resulting in a significantly high carrier density on the surface. These results are expected to provide a new strategy for tuning the carrier density of p-type organic semiconductors, which will be beneficial for organic electronics, materials science, and other related fields.

1. Introduction

Organic semiconductors have several disadvantages that render them inferior to their inorganic counterparts. One of the most significant disadvantages is their low carrier mobility.[1] Over the last three decades, however, we have witnessed marked carrier mobility improvements in organic semiconductors,[2–4] from

[a] *RIKEN Center for Emergent Matter Science (CEMS), 2-1 Hirosawa, Wako, Saitama 351-0198, Japan. E-mail: takimiya@riken.jp*
[b] *Department of Chemistry, Graduate School of Science, Tohoku University, 6-3 Aoba, Aramaki, Aoba-ku, Sendai, Miyagi 980-8578, Japan*
[c] *Tohoku University Advanced Institute for Materials Research (AIMR), 2-1-1 Katahira, Aoba-ku, Sendai, Miyagi 980-8577, Japan*

field-effect mobility of the order of $\sim 10^{-5}$ cm^2 V^{-1} s^{-1} reported for the first organic field-effect transistors (OFETs)[5] to several tens cm^2 V^{-1} s^{-1} recently reported for the state-of-the-art OFETs.[6–11] Another disadvantage is their low carrier density,[12–14] which originates in the closed-shell electronic structure of organic semiconductor molecules. A low carrier density may be beneficial for applying active semiconducting materials in OFETs. However, it can pose a significant disadvantage in other device applications, such as carrier transport materials used in photovoltaic and thermoelectric devices. To address this issue, molecular doping—charge transfer between a dopant and a host organic semiconductor—was developed.[13]

On the other hand, the spontaneous air-doping of p-type organic semiconductors having high-lying HOMO energy levels at the single molecular level (E_{HOMO}) is often observed.[15–18] This "unwilling doping" is generally uncontrollable for p-type organic semiconductors with E_{HOMO} higher than 5.0 eV below the vacuum level (VL) and is one of the causes of p-channel OFET degradation.[19] For this reason, lowering E_{HOMO} is critical in the design of air-stable p-type organic semiconductors.[20] The optimal E_{HOMO} values of organic semiconductors are 5.0–5.5 eV below the VL. Dinaphtho[2,3-b:2′,3′-f]thieno[3,2-b]thiophene (DNTT; Fig. 1a)

is a representative thienoacene-based organic semiconductor that acts as an excellent channel material for the fabrication of stable and high-performance OFETs.[21,22] The stability of DNTT in ambient air is due to its low-lying E_{HOMO} ($\sim$5.4 eV below the VL), which prevents unwilling doping. Reliable DNTT-based integrated circuits have been utilized in state-of-the-art flexible devices.[23-26] Molecular modifications of DNTT have also afforded promising materials with high mobility, thermal stability, and solution processability. Recently developed 2-bromodinaphtho[2,3-b:2′,3′-f]thieno[3,2-b]thiophene (Br–DNTT; Fig. 1a) is a versatile reactant in cross-coupling reactions that yields solution-processable DNTT derivatives.[27-29] To further extend the cross-coupling chemistry, we converted Br–DNTT into the corresponding pinacolborane-substituted DNTT: 2-(4,4,5,5-tetramethyl-1,3,2-dioxaborolan-2-yl)dinaphtho[2,3-b:2′,3′-f]thieno[3,2-b]thiophene (Bpin–DNTT; Fig. 1a).

Besides its role as a key reactant in the Suzuki–Miyaura cross-coupling reaction, Bpin–DNTT is useful as an active material in thin-film transistors (TFTs), showing ideal normally-off behavior with a mobility of up to 2.5 cm^2 V^{-1} s^{-1}. Intriguingly, the Bpin–DNTT-based TFTs are extremely sensitive to ambient air despite the low-lying E_{HOMO} of Bpin–DNTT ($\sim$5.4 eV below the VL). To clarify this unexpected behavior, we evaluated Bpin–DNTT through single-crystal field-effect transistor (SC-FET), electron spin resonance (ESR) spectroscopy, ultraviolet photoelectron spectroscopy (UPS), and theoretical calculations. We conclude that the Bpin group has a hitherto unknown function—it significantly reduces the ionization energy (IE) in the solid state.

2. Methods

2.1 Synthesis of Bpin–DNTT

4,4,4′,4′,5,5,5′,5′-Octamethyl-2,2′-bi(1,3,2-dioxaborolane) (54 mg, 0.21 mmol), Br–DNTT[27] (29 mg, 0.070 mmol), and palladium acetate (0.30 mg, 0.0013 mmol) were added to a Schlenk tube. The Schlenk tube was evacuated, backfilled with argon gas, and
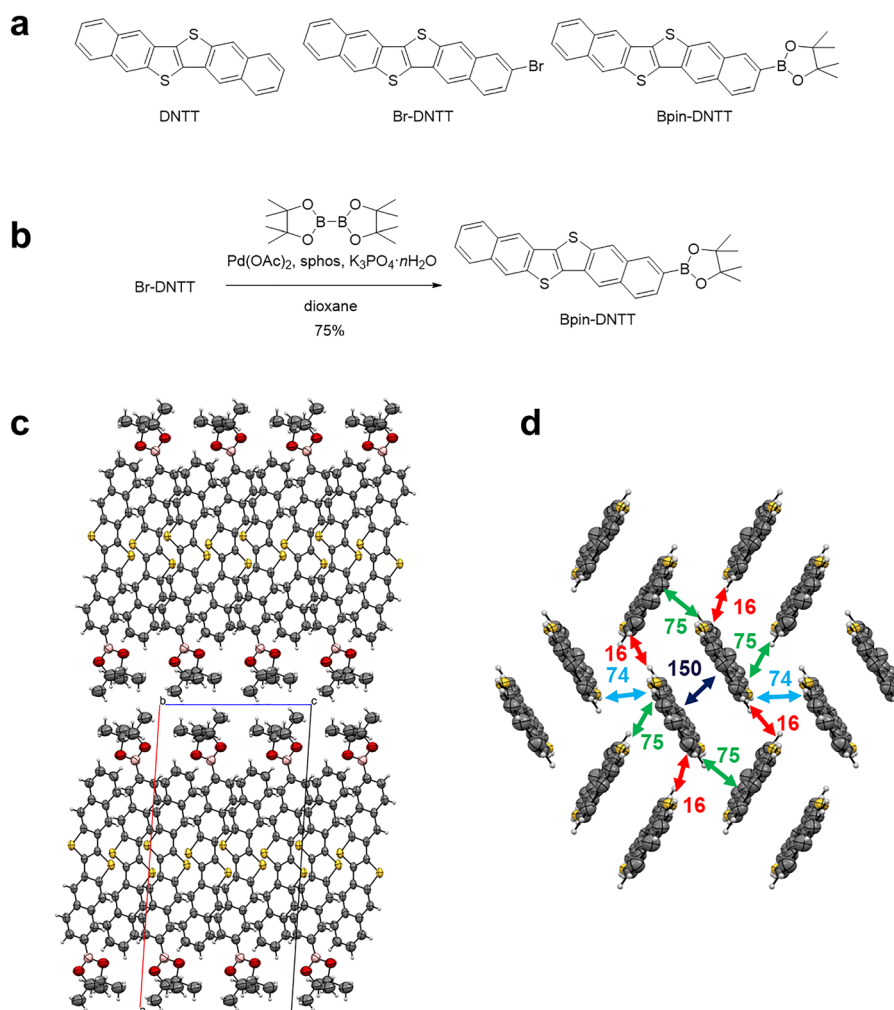

Fig. 1 Chemical structures, synthesis, and crystal structure. (a) Chemical structures of DNTT, Br–DNTT, and Bpin–DNTT. (b) Synthesis of Bpin–DNTT. (c) Crystal structure of Bpin–DNTT (CCDC-2372480) viewed along the crystallographic b-axis, representing the layered structure of the DNTT part separated by Bpin groups. (d) A sandwich herringbone arrangement in the DNTT layer (a-axis projection) with the calculated intermolecular electronic couplings of HOMOs (meV). For clarity, the Bpin groups are omitted.

then kept under a nitrogen atmosphere. 1,4-Dioxane (2 mL, purified by distillation) was added *via* syringe. The reaction mixture was heated to 110 °C for 37 hours. After the reaction mixture was allowed to cool to room temperature, it was subjected to chromatography on silica gel (eluent: toluene) and purified by reprecipitation from a hexane/toluene mixed solvent to yield Bpin–DNTT as yellow microcrystals (17 mg, 51%). Mp 363.5 °C (DSC peak temperature). ^{1}H NMR (CDCl$_3$, 500 MHz): δ (ppm) 8.48 (s, 1H), 8.45 (s, 1H), 8.42 (s, 1H), 8.38 (s, 1H), 8.35 (s, 1H), 8.05–8.03 (m, 1H), 8.01 (d, J = 9.0 Hz, 1H), 7.96–7.94 (m, 1H), 7.87 (dd, J = 8.0, 1.0 Hz, 1H) 7.55–7.52 (m, 2H), 1.42 (s, 12H). ^{13}C NMR (CDCl$_3$, 125 MHz): δ (ppm) 140.89, 140.69, 135.91, 134.42, 133.84, 133.23, 132.68, 132.36, 131.56, 131.28, 130.86, 130.07, 128.35, 127.37, 127.32, 125.99, 125.70, 123.33, 122.47, 120.29, 119.97, 84.07, 24.99 (a signal from the *ipso*-carbon atom to the pinacolborane group was too weak to be observed probably due to the quadrupole moments of the boron nuclei). HRMS (FD) *m*/*z*: calcd. for C$_{28}$H$_{23}$B$_1$O$_2$S$_2$ [M]$^+$: 466.1237. Found: 466.1230. Anal. calcd. for C$_{28}$H$_{23}$B$_1$O$_2$S$_2$: C, 72.10; H, 4.97%. Found: C, 72.34; H, 4.99%.

2.2 Single-crystal X-ray analysis

Single crystals of Bpin–DNTT were grown by recrystallization from hexane-toluene or by the physical-vapor-transport (PVT) method. Single-crystal X-ray structural analyses were carried out using a Rigaku Oxford Diffraction XtaLAB Synergy Custom DW system with a HyPix-6000HE detector (CuKα radiation, wavelength: 1.5418 Å, multilayer confocal optics). The structures were solved by the SHELXT program.[30] Non-hydrogen atoms were refined anisotropically.[31] All calculations were carried out by using the crystallographic software package Olex2 (ver. 1.5.0).[32] Crystal data: yellow plate, monoclinic, $P2_1/c$, a = 25.0771(19), b = 7.6507(4), c = 12.2423(5) Å, β = 93.709(5)°, V = 2343.9(2) Å^3, Z = 4, T = 293(2) K, R = 0.0762 (3308), wR^2 = 0.2493(4623), GOF = 1.056 (CCDC-2372480).† X-ray diffraction patterns of evaporated thin films of Bpin–DNTT on Si/SiO$_2$ substrates were recorded using a Rigaku Ultima IV with CuKα radiation (wavelength: 1.54184 Å).

2.3 Theoretical calculations

By using the Gaussian 16 program package, the molecular structure optimization and the estimation of energy levels of the frontier molecular orbitals and g tensors were carried out at the B3LYP/6-311G(d) level for the neutral state and the UB3LYP/6-311G(d,p) level for the radical cationic state.[33] Intermolecular electronic coupling (transfer integral, t) in different molecular dimers extracted from the crystal structure was calculated with the Amsterdam density functional (ADF) program.[34] Intermolecular interaction energies for dimers of Bpin–DNTT and DNTT extracted from the crystal structures were calculated by SAPT methods[35] with the jun-cc-pvdz level using the PSI4 program package.[36] Band structure calculations and electrostatic potential calculations for DNTT and Bpin–DNTT crystals with the geometries determined by single-crystal X-ray analysis were carried out with three- or two-dimensional periodic boundary conditions with the CRYSTAL17 program package

by the plane-wave DFT method at the B3LYP/6-31G(d,p) level of theory, where a shrinking factor of 12 for the Pack–Monkhorst net was used.[37]

2.4 Fabrication of TFTs and SC-FETs

Onto octylsilane (OTS)-treated Si/SiO$_2$ substrates, Bpin–DNTT or DNTT thin films (30 nm) were vacuum-deposited under 10^{-4} Pa with a deposition rate of 0.1 Å s^{-1} at a substrate temperature of 100 °C for Bpin–DNTT and 60 °C for DNTT. On top of the thin films, gold drain and source contact electrodes (thickness: 40 nm) with a channel length of 100 μm and a width of 1500 μm, respectively, were vacuum-deposited through shadow masks under a pressure of 10^{-4} Pa.

For SC-FETs, heavily doped n-type Si wafers with thermally grown SiO$_2$ layers ($\sim$200 nm) were used as substrates. The wafers were cleaned by sonication in acetone for 10 min twice, followed by ultraviolet-ozone treatment for more than 30 min. The wafers were spin-coated with 3 wt% CYTOP (AGC) solution in CT-Solv.180 (AGC) at 3000 rpm for 1 min and dried at 180 °C on a hot plate in air. The thickness of the CYTOP film ($\sim$90 nm) was measured using AFM (NanoNavi IIs/NanoCute).

Single crystals of Bpin–DNTT were grown from purified powder samples using the PVT method under a nitrogen carrier gas flow. The resulting single crystals were carefully transferred to the surface of the CYTOP film using a tungsten needle. The top-contact SC-FETs were completed by placing droplets of water-based colloidal graphite on each side of the crystals as the source and drain electrodes. All FET measurements were performed in air using a probe station and a semiconductor parameter analyzer (Keithley 4200-SCS). The carrier mobility was calculated from the forward swing of the transfer characteristics by using the following equation:

$$|I_d| = \frac{W}{2L} C_i \mu \left(V_g - V_{th} \right)^2,$$

where L and W are the channel length and width of the FETs, respectively, C_i is the gate dielectric capacitance per unit area, and V_{th} is the threshold voltage. C_i of the CYTOP/SiO$_2$ layers was determined to be 8.7–9.0 nF cm^{-2} by using an Au electrode (2.5 × 1.5 mm^2) deposited on the CYTOP surface.

2.5 ESR spectra

ESR spectra were measured using a Bruker Magnettech ESR5000 spectrometer at room temperature with an operating frequency of 9.4 GHz. Evaporated thin films of Bpin–DNTT and DNTT on OTS-treated glass substrates (3 × 16 mm^2, four sheets) were placed in a natural quartz tube with a 5 mm diameter. The number of spins was calculated by double integration of the spectra using the ESRStudio software package, where the spectra of a TEMPO solution (10^{-4} mol L^{-1}) in toluene measured under the same conditions were used as the external standard. The amount of spin was divided by the total surface area (192 mm^2) on the thin film to give the spin density per area. ESR spectra of a chloroform solution of Bpin–DNTT (3.7 mmol L^{-1}) showed no significant signal (blue line in Fig. S8a). On the other hand, the solid sample, after

evaporating the chloroform in the sample tube, showed a clear signal (red line in Fig. S8a).

2.6 Ultraviolet photoelectron spectroscopy (UPS)

UPS measurements were performed with a photoelectron spectroscopy system (PHI5000 VersaProbe II, ULVAC-PHI Inc.) with He I excitation (21.2 eV). Total energy resolution was 120 meV at room temperature. The bare Si or Au substrates used in the measurements were connected to the sample holder with conductive silver paste to ensure thermodynamic equilibrium (Fig. S9a). A −5.0 V bias was applied to the samples. All the measurements were carried out at room temperature with a pressure of approximately 1×10^{-6} Pa.

3. Results and discussion

3.1 Synthesis and characterization

Bpin–DNTT was synthesized *via* a typical Miyaura–Ishiyama borylation reaction of Br–DNTT and bis(pinacolato)diboron in 51% isolated yield (Fig. 1b).[38] Bpin–DNTT is a thermally stable compound whose decomposition temperature is above 300 °C. Bpin-DNTT can be vacuum-evaporated to form uniform thin films on various substrates. The Bpin group in the DNTT core

acts as a solubilizing group, markedly improving solubility in chloroform at room temperature (2.7 g L^{-1}), which enables solution deposition of thin films on substrates.[27,29] The cyclic voltammogram of Bpin–DNTT is characterized by a quasi-reversible oxidation peak with an onset peak at 0.65 V against the Fc/Fc$^+$ redox couple, corresponding to E_{HOMO} of 5.45 eV (DNTT: 5.43 eV) below the VL, in good agreement with the DFT calculation results (Fig. S3). The low-lying E_{HOMO} of Bpin–DNTT is expected to ensure stability in ambient air, similar to the parent DNTT and its derivatives.

3.2 Molecular arrangement in the solid state

Similar to the molecular arrangement of DNTT, Bpin–DNTT forms a layer-by-layer structure of the DNTT core in its crystal structure, as determined by single-crystal X-ray structural analysis (Fig. 1c). The molecular arrangement in the DNTT layer is, however, characterized by a sandwich herringbone structure (Fig. 1d), markedly different from the parent DNTT with a herringbone structure. A similar sandwich herringbone structure was observed for (triisopropylsilyl)ethynyl–DNTT,[28] indicating that bulky substituents can alter the crystal structure from the herringbone to the sandwich herringbone structure. The sandwich herringbone structure was maintained in thin
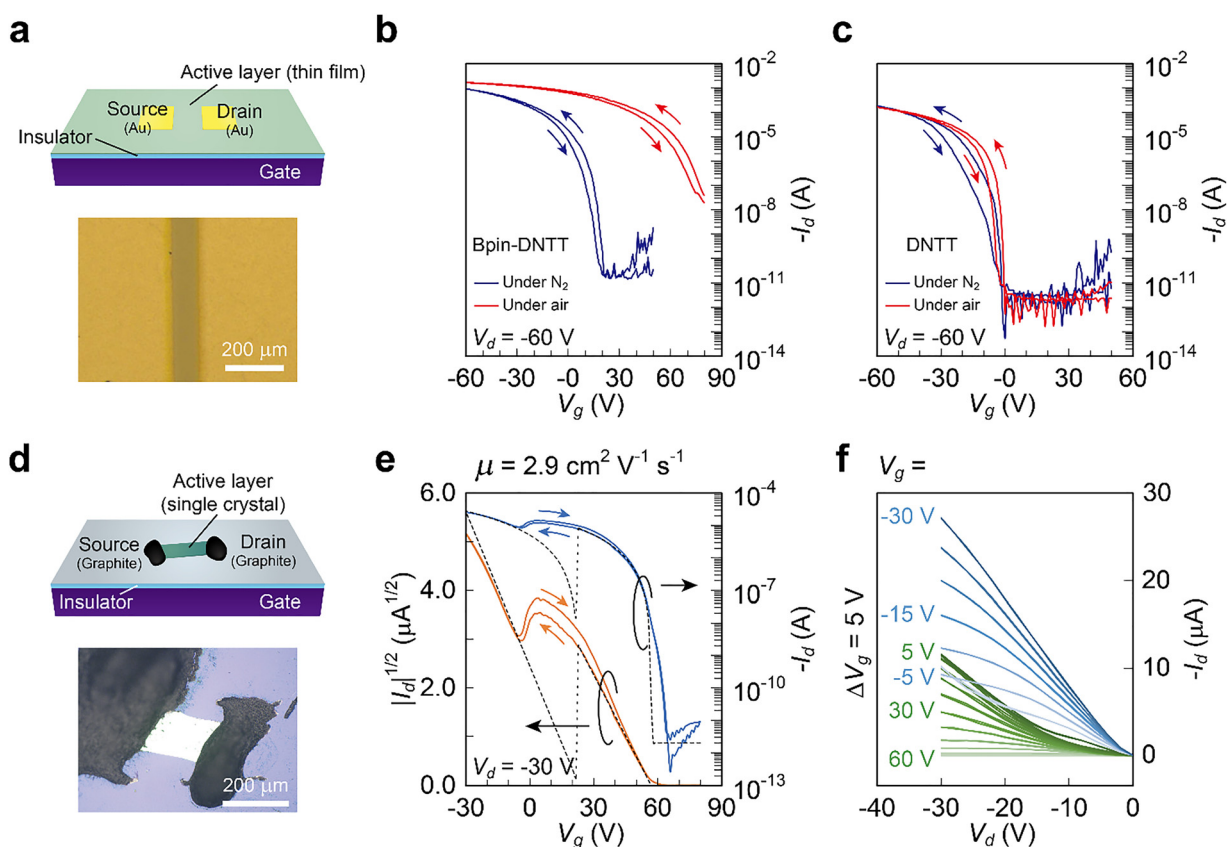

Fig. 2 Field-effect transistors. (a) Schematic of the device structure of a bottom-gate, top-contact TFT, and a photograph of the device. (b) and (c) Transfer curves of Bpin–DNTT- and DNTT-based TFTs fabricated on OTS-modified substrates, respectively. The blue trace was that recorded under N$_2$, and the red trace was obtained after exposure to ambient air. (d) Schematic of the device structure of SC-FET and a photograph of the device. (e) and (f) Transfer and output curves of Bpin–DNTT-based SC-FET, respectively, with simulated transfer curves postulating the overlap of two independent transistors.

films on Si/SiO_2 substrates, judging from the out-of-plane and in-plane thin-film X-ray diffraction (XRD) patterns. In the in-plane XRD pattern, four peaks characteristic of the sandwich herringbone structure were observed (Fig. S5).

We estimated the intermolecular transfer integrals of the HOMOs on the basis of the crystal structure (Fig. 1d). Along with the largest transfer integral ($\sim$150 meV) calculated for the *anti*-parallel Bpin–DNTT dimer, relatively large transfer integrals between the dimers ($\sim$75 meV in two directions) enabled a two-dimensional (2D) interactive electronic structure in the semiconducting layer, which was suitable for efficient carrier transport (*vide infra*).

3.3 Thin-film transistors

The Bpin–DNTT thin films were fabricated by spin-coating from a chloroform solution or vacuum deposition on Si/SiO_2 substrates. On top of the thin films, gold source and drain electrodes were vacuum-deposited through a shadow mask to define the source and drain electrodes (Fig. 2a). All the device fabrication processes through the solution and the vacuum deposition methods were conducted under air-free conditions. Fig. 2b (blue trace) shows the transistor characteristics of the Bpin–DNTT-based TFTs with the vapor-deposited thin film. The extracted mobility from the saturation regime ($V_d = -60$ V) is as high as 2.5 cm^2 V^{-1} s^{-1} (0.1 cm^2 V^{-1} s^{-1} for the solution-processed devices; Fig. S4) and comparable to that for the DNTT-based TFTs (Fig. 2c). Such high mobility could be rationalized by the 2D electronic structure with large intermolecular transfer integrals of the HOMOs (Fig. 1d).

However, these superior transistor characteristics were drastically changed upon exposure to ambient air. Once the devices were taken out of the nitrogen-filled glovebox, a significantly large threshold voltage (V_{th}) shift was observed, resulting in no clear off-state (Fig. 2b, red trace). This phenomenon could be understood by considering air oxidation; thermoelectric measurements of the Bpin–DNTT thin film after exposure to ambient air revealed that the active carrier species were holes (see SI, Fig. S6). Although similar hole doping has been reported in p-type organic semiconductors with E_{HOMO} higher than 5.0 eV below the VL,[19] this result was puzzling as the electrochemical and theoretically estimated E_{HOMO} values were approximately 5.4 eV below the VL, which should be sufficiently low lying for E_{HOMO} of "air-stable" p-type organic semiconductors. Note that the TFT of parent DNTT with an E_{HOMO} of approximately 5.4 eV below the VL did not show such an increase of I_d at $V_g = 0$ V upon exposure to ambient air (Fig. 2c, red trace).

3.4 Single-crystal field-effect transistors

The evaporated Bpin–DNTT thin films consisted of crystalline grains (or crystallites; Fig. S7); thus, the grain boundary could affect the transistor characteristics of the TFTs. SC-FETs could exclude the effects of the grain boundary and be used to assess the intrinsic transport properties. Thus, SC-FETs were fabricated with vapor-grown single crystals of Bpin–DNTT with a *ca.* 150 nm thickness (Fig. 2d). Note that single crystals were grown

in an air-free environment, and the device fabrication of Bpin–DNTT SC-FETs was performed in air.

In contrast to the transfer curves of the Bpin–DNTT TFTs after exposure to ambient air (Fig. 2b, red trace), where no complete depletion was confirmed even with a very large positive V_g (up to +80 V), an almost complete off-state was confirmed in the transfer curves of the SC-FETs (Fig. 2e). More intriguingly, the transfer curves of the SC-FETs exhibited a double-slope behavior with a negative transconductance region,[39–41] where two independent transistors operated at different V_g ranges in the SC-FETs; one transistor operated at $V_g < 0$ V and the other at $V_g > 0$ V, and an apparent dip was observed at approximately $V_g = 0$ V in the square root of I_d ($|I_d|^{1/2}$; orange trace in Fig. 2e). The output characteristics supported the "dual transistor"-like behavior; two series of output curves (blue and green traces) were observed (Fig. 2f). The output curves of the first transistor (blue traces) did not show clear saturation at high V_d, indicating that the transistor is affected by the contact resistance. On the other hand, those of the second transistor (green traces) at $V_g = 5$–15 V show a kink, implying the contact is not ohmic and V_d-dependent. Nevertheless, to understand the dual transistor-like behavior, we considered the following simplified model, neglecting contact characteristics: the channel of the first transistor exists at the interface between the substrate and the crystal, and that of the second transistor exists on the crystal's surface (interface between the crystal and air). The first transistor was turned on by applying a negative gate bias ($V_g < 0$ V) as an ordinary enhancement-type p-channel FET. On the other hand, the second transistor, where hole carriers exist at $V_g = 0$ owing to air oxidation, behaved as a depletion-type FET. The hole carriers in the latter FET could be depleted by applying a large positive gate bias ($V_g \sim$ +60 V), realizing the complete off-state of the whole SC-FET. Based on the dual-transistor model, a simulation was carried out by assuming the overlap of two independent transistors (Fig. 2f): one transistor ($\mu = 2.9$ cm^2 V^{-1} s^{-1}, $V_{th} = $ +21 V, $C_i = 8.9$ nF) was at the interface between the crystal and the substrate, and the other ($\mu = 2.9$ cm^2 V^{-1} s^{-1}, $V_{th} = $ +57 V, $C_i = 6.0$ nF) was on the crystal's surface. The difference in capacitance corresponded to a crystal of *ca.* 150 nm thickness, acting as an additional gate insulator with a relative permittivity of 3. The superposed transfer curves of the models, shown as dotted lines in Fig. 2e, fit the experimental transfer curves, indicating that the dual-transistor model is plausible.

3.5 ESR spectroscopy and estimation of carrier density in Bpin–DNTT

As discussed above, the active carriers at $V_g = 0$ V in both TFTs and SC-FETs after exposure to ambient air were holes. This meant that the Bpin–DNTT thin films and single crystals were oxidized to generate radical cations that should be ESR-active. The ESR spectra of the evaporated Bpin–DNTT thin films exposed to ambient air showed a clear peak at $g = 2.00465$, indicating the existence of radical cations in the Bpin–DNTT thin film (Fig. 3a).[42,43] Note that the air-saturated solution of Bpin–DNTT in chloroform was ESR-silent (Fig. S8). The parent

DNTT thin films exposed to ambient air were also ESR-silent (Fig. 3a). These results indicated that (i) in solution, Bpin–DNTT was "air-stable" like DNTT, consistent with the results of the electrochemical E_{HOMO} of Bpin–DNTT, and (ii) Bpin–DNTT was readily oxidized to generate radical cations in the solid state.

The ESR spectra of the evaporated thin films of different thicknesses after exposure to ambient air (20, 40, and 60 nm; Fig. 3b) showed no clear dependence of the peak intensity on the film thickness. This implies that active carriers are generated only on the surface of the thin films. The estimated spin density (carrier density) in the evaporated thin films was 1×10^{13} cm^{-2}. Provided that the molecules only in the first monolayer (ca. 25 Å, the length of the crystallographic a-axis) of the surface were oxidized, the carrier density was estimated to be 4×10^{19} cm^{-3}. This high carrier density is within the range (10^{18} to 10^{21} cm^{-3}) for which maximum conductivity can be realized in organic semiconductors.[44–46]

We also estimated the carrier density from the transistor characteristics. With the drain current (I_d) at $V_g = 0$ in the transfer curve of the TFTs after exposure to ambient air (Fig. 2b, red trace), the resistivity of the Bpin–DNTT channel ($L = 100$ mm, $W = 1500$ mm) was calculated to be ca. 0.59 Ω cm, assuming that only the first monolayer of the surface contributed to the electrical conductivity. With the carrier mobility extracted from the TFT (μ, 2.5 cm^2 V^{-1} s^{-1}) and the elementary charge (q, 1.602×10^{-19} C), the carrier density was estimated to be approximately 4.2×10^{18} cm^{-3}. Like the TFT case, the carrier density in the surface monolayer of the SC-FET, estimated from I_d at $V_g = 0$, was approximately 3.6×10^{18} cm^{-3}. These values are slightly lower than those determined from the ESR spectra but are almost consistent, confirming that the carrier density in Bpin–DNTT solid is significantly higher than that in ordinary organic semiconductors.

3.6 Ultraviolet photoelectron spectroscopy

The absence of an off-state in the Bpin–DNTT-based TFTs after exposure to ambient air could be explained by the high carrier density in the air-doped surface. This was in sharp contrast to DNTT that yielded air-stable TFTs (Fig. 2c). What was puzzling was that the electrochemical E_{HOMO} values of these two compounds were almost identical and sufficiently low as air-stable organic semiconductors. These imply that there are differences in the solid-state electronic structures of the two compounds. To elucidate the solid-state electronic structures, UPS measurement of the Bpin–DNTT thin film, together with the DNTT thin film as reference, on Si substrate with native oxide on the surface (hereafter bare Si) was performed.

The UPS spectra of DNTT and Bpin–DNTT thin films deposited on bare Si substrates are shown in Fig. 4a and b, respectively. The IE of the DNTT thin film was determined to be 5.18 eV, closer to the reported value of a DNTT single crystal (5.02 eV)[47] than that of an evaporated thin film on an Au substrate (5.44 eV) (see SI and Fig. S9).[48] This is likely due to the higher crystallinity of DNTT on the bare Si substrate than on the Au substrate (Fig. S7). Fig. 4a and b show that the IE values of Bpin–DNTT (4.58 eV) and DNTT (5.18 eV) differ by 0.6 eV. It is known that through ordering in the solid state, the IEs of organic semiconductors often shift from their E_{HOMO} evaluated by electrochemical methods. As observed in the present DNTT case, the IE (5.18 eV) shifted from 5.4 eV (determined by an electrochemical method), but the difference is only approximately 0.2 eV. In the Bpin–DNTT case, the difference is unusually large (ca. 0.9 eV), resulting in a very small IE of 4.58 eV. Thus, the small IE of the Bpin–DNTT solid is the primary reason for the air-doping of its TFTs and SC-FETs.

3.7 Origin of the large IE shift in Bpin–DNTT thin film

The energy diagrams aligned with respect to the Fermi level (E_F) show that the IE shift of Bpin–DNTT from that of DNTT can be deconvoluted into a downward VL shift of 0.37 eV and an upward valence band top edge (HOMO band) shift of 0.23 eV (Fig. 4c left). The VL shift of the crystal surfaces in organic semiconductors is primarily attributed to the surface dipoles, as described in the literature. A previous study reported only upward VL shifts induced mainly by the fluorination of the semiconducting core, where a strong surface dipole moment from the air side to the crystal side originates from highly polarized carbon–fluorine bonds that have an opposite polarity to carbon–hydrogen bonds.[49] With this mechanistic framework, the observed downward VL shift from DNTT to Bpin–DNTT indicates that the local dipole moments of the
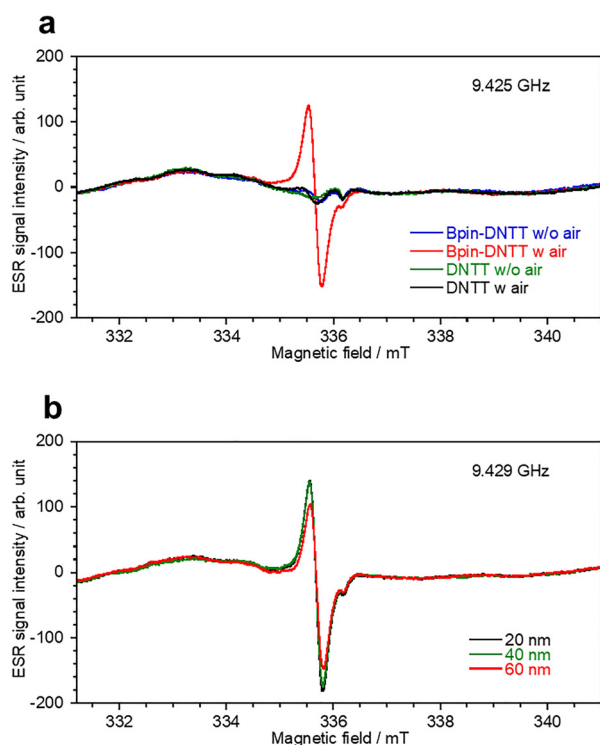
Fig. 3 ESR spectra of Bpin–DNTT and DNTT thin films. (a) ESR spectra before and after exposure to ambient air. (b) ESR spectra of Bpin–DNTT thin films with different thicknesses after exposure to ambient air. The experimental g value, 2.00465, agrees well with the theoretically calculated one (2.00432) (see SI).
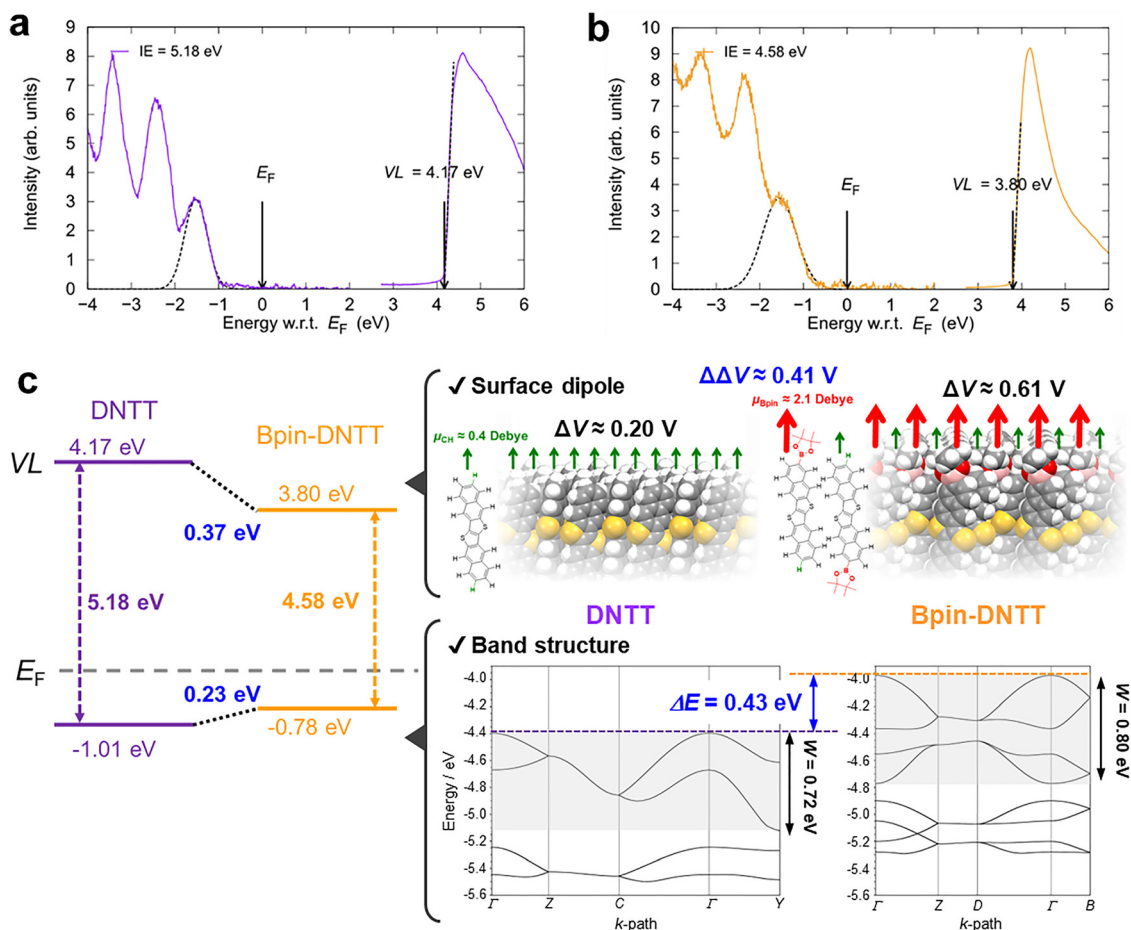
Fig. 4 Solid-state electronic structures of Bpin–DNTT and DNTT. (a) and (b) UPS spectra of DNTT and Bpin–DNTT thin films deposited on bare Si substrates, respectively. (c) Energy diagrams of Bpin–DNTT and DNTT. The large IE shift can be deconvoluted into the VL shift (0.37 eV) and the shift of the HOMO band edge (0.23 eV). Schematic representation of the impact of Bpin groups aligned on the surface of Bpin–DNTT solid on the crystallographic *bc*-plane. A large surface dipole (ΔV) is induced, resulting in the VL shift. Calculated HOMO bands (gray background) of Bpin–DNTT (right) and DNTT (left), showing a HOMO band edge difference (ΔE) of 0.43 eV.

C–Bpin moiety on the crystal surface point from the crystal side to the air side, their strengths being greater than the C–H bond dipole moments in DNTT. Indeed, the local dipole moment of the C–Bpin moiety was estimated to be approximately 2.1 D in the direction from the C to the Bpin group, much stronger than a typical C–H bond dipole moment (0.40 D) (see SI). The Bpin–DNTT crystal surface (*bc* plane) has C–Bpin and C–H moieties pointing to the air side, whereas the DNTT crystal surface (*ab* plane) has an array of only C–H moieties. Based on the Helmholtz equation, the electrostatic potential shift (ΔV) due to the surface dipole moments can be calculated by the following equation:[50,51]

$$\Delta V = \frac{N_{\text{dipole}} \mu_z}{\varepsilon_0 \varepsilon_{\text{norm}}}$$

where N_{dipole} is the number of molecular dipoles per unit area, μ_z is the perpendicular component of the surface dipole moment of molecules with respect to the crystallographic *bc* plane (Bpin–DNTT) or the *ab* plane (DNTT), ε_0 is the vacuum permittivity, and $\varepsilon_{\text{norm}}$ is the relative permittivity of ordinary

organic molecules (= 3). The estimated ΔV values for Bpin–DNTT and DNTT are *ca.* 0.61 and 0.20 V, respectively, and their difference ($\Delta\Delta V$ = 0.41 V) qualitatively agrees with the VL shift experimentally obtained (see SI). Thus, we conclude that the strong local dipole moment of the C–Bpin moiety is responsible for the downward VL shift (Fig. 4c, upper right).

On the other hand, band calculations based on the crystal structures demonstrate a clear difference in the band edge of the valence band between DNTT and Bpin–DNTT, although their bandwidths (W) are almost the same (Fig. 4c, lower right). The calculated energetic difference in the band edges is 0.43 eV, which qualitatively agrees with the value estimated by UPS measurements (0.23 eV). The origin of such a large difference can be related to the strong dimerization of Bpin–DNTT (Fig. 1d), which effectively elevates the E_{HOMO} of molecular clusters (Fig. S14 and S15).[52] The strong dimerization of Bpin–DNTT in an *anti*-parallel face-to-face manner, promoting the effective overlap of molecular orbitals, is the outcome of the large molecular dipole induced by the Bpin group on the DNTT core (see SI). From the results of experiments and theoretical

calculations, we conclude that the Bpin group is the origin of both the downward VL shift and the upward shift of the HOMO band edge in the solid state.

4. Conclusions

We experimentally found that the Bpin–DNTT-based TFTs were easily hole-doped despite the low-lying electrochemical E_{HOMO}. SC-FET and ESR studies confirmed that the surface of the Bpin–DNTT solid was easily doped, and the carrier density in the surface monolayer reached $\sim 10^{19}$ cm^{-3}. Such spontaneous doping of the surface was the outcome of the extremely small IE of the Bpin–DNTT solid, experimentally confirmed by UPS. Theoretical calculations of the electronic structure of the surface and the bulk of Bpin–DNTT crystal suggested that such a small IE comes from the downward shift of VL and the upward shift of the HOMO band edge. These significant effects of the Bpin group on the solid-state electronic structure were elucidated for the first time, even though a substantial number of Bpin-modified π-conjugated molecules have been reported. Furthermore, no functional groups that induce the downward VL shift, in contrast to the upward shift induced by fluorine groups, have been reported.

The phenomena reported in the present work show that the Bpin group, a functional group exclusively used as a workhorse functional group in the Suzuki–Miyaura cross-coupling reaction, could be an unprecedented tool for tuning the low carrier density in p-type organic semiconductors. In fact, a similar IE shift was also observed in a related molecule, Bpin-modified [1]benzothieno[3,2-b]naphtho[2,3-b]thiophene (Fig. S16), with a similar crystal structure, though the resulting IE is not low enough for air doping, owing to a less π-extended core with a low-lying HOMO energy level at the molecular level. The appropriate design of Bpin-modified organic semiconductors will be a new molecular design strategy to solve the issue of low carrier density in p-type organic semiconductor solids.

Author contributions

K. Takimiya and K. K. conceived and designed the project. S. U. and R. H. synthesized Bpin–DNTT, and fabricated and evaluated TFTs. K. B. and K. Takimiya grew single crystals and solved the structure. K. B. prepared SC-FETs and evaluated the performances. K. N. and K. Tajima conducted UPS measurements. K. K. and K. B. performed theoretical calculations. K. Takimiya and K. K. co-wrote the manuscript with contributions from all coauthors.

Conflicts of interest

There are no conflicts to declare.

Data availability

The experimental and analytical methods described in the paper are available from the corresponding authors upon reasonable request.

Supplementary information (SI): experimental and computational details, simulated crystal structures. See DOI: https://doi.org/10.1039/d5mh01969a.

CCDC 2372480 and 2519941 contain the supplementary crystallographic data for this paper.[53a,b]

Notes and references

† Experimental crystallographic data for Bpin–DNTT (CCDC-2372480).

1 V. Coropceanu, J. Cornil, D. A. da Silva Filho, Y. Olivier, R. Silbey and J.-L. Brédas, Charge Transport in Organic Semiconductors, *Chem. Rev.*, 2007, **107**, 926–952.

2 C. Wang, H. Dong, W. Hu, Y. Liu and D. Zhu, Semiconducting π-Conjugated Systems in Field-Effect Transistors: A Material Odyssey of Organic Electronics, *Chem. Rev.*, 2012, **112**, 2208–2267.

3 J. Mei, Y. Diao, A. L. Appleton, L. Fang and Z. Bao, Integrated Materials Design of Organic Semiconductors for Field-Effect Transistors, *J. Am. Chem. Soc.*, 2013, **135**, 6724–6746.

4 H. Sirringhaus, 25th Anniversary Article: Organic Field-Effect Transistors: The Path Beyond Amorphous Silicon, *Adv. Mater.*, 2014, **26**, 1319–1335.

5 A. Tsumura, H. Koezuka and T. Ando, Macromolecular electronic device: Field-effect transistor with a polythiophene thin film, *Appl. Phys. Lett.*, 1986, **49**, 1210–1212.

6 V. Podzorov, E. Menard, A. Borissov, V. Kiryukhin, J. A. Rogers and M. E. Gershenson, Intrinsic Charge Transport on the Surface of Organic Semiconductors, *Phys. Rev. Lett.*, 2004, **93**, 086602.

7 J. Takeya, M. Yamagishi, Y. Tominari, R. Hirahara, Y. Nakazawa, T. Nishikawa, T. Kawase, T. Shimoda and S. Ogawa, Very high-mobility organic single-crystal

transistors with in-crystal conduction channels, *Appl. Phys. Lett.*, 2007, **90**, 102120.

8 C. Mitsui, T. Okamoto, M. Yamagishi, J. Tsurumi, K. Yoshimoto, K. Nakahara, J. Soeda, Y. Hirose, H. Sato, A. Yamano, T. Uemura and J. Takeya, High-performance solution-processable N-shaped organic semiconducting materials with stabilized crystal phase, *Adv. Mater.*, 2014, **26**, 4546–4551.

9 H. Iino, T. Usui and J.-I. Hanna, Liquid crystals for organic thin-film transistors, *Nat. Commun.*, 2015, **6**, 6828.

10 D. Ji, T. Li, J. Liu, S. Amirjalayer, M. Zhong, Z.-Y. Zhang, X. Huang, Z. Wei, H. Dong, W. Hu and H. Fuchs, Band-like transport in small-molecule thin films toward high mobility and ultrahigh detectivity phototransistor arrays, *Nat. Commun.*, 2019, **10**, 12.

11 K. Takimiya, K. Bulgarevich, M. Abbas, S. Horiuchi, T. Ogaki, K. Kawabata and A. Ablat, ''Manipulation'' of Crystal Structure by Methylthiolation Enabling Ultrahigh Mobility in a Pyrene-Based Molecular Semiconductor, *Adv. Mater.*, 2021, **33**, 2102914.

12 I. Salzmann, G. Heimel, M. Oehzelt, S. Winkler and N. Koch, Molecular Electrical Doping of Organic Semiconductors: Fundamental Mechanisms and Emerging Dopant Design Rules, *Acc. Chem. Res.*, 2016, **49**, 370–378.

13 B. Lüssem, C.-M. Keum, D. Kasemann, B. Naab, Z. Bao and K. Leo, Doped Organic Transistors, *Chem. Rev.*, 2016, **116**, 13714–13751.

14 I. E. Jacobs and A. J. Moulé, Controlling Molecular Doping in Organic Semiconductors, *Adv. Mater.*, 2017, **29**, 1703063.

15 M. S. A. Abdou, F. P. Orfino, Y. Son and S. Holdcroft, Interaction of Oxygen with Conjugated Polymers: Charge Transfer Complex Formation with Poly(3-alkylthiophenes), *J. Am. Chem. Soc.*, 1997, **119**, 4518–4524.

16 S. Ogawa, T. Naijo, Y. Kimura, H. Ishii and M. Niwano, Photoinduced doping effect of pentacene field effect transistor in oxygen atmosphere studied by displacement current measurement, *Appl. Phys. Lett.*, 2005, **86**, 252104.

17 H.-H. Liao, C.-M. Yang, C.-C. Liu, S.-F. Horng, H.-F. Meng and J.-T. Shy, Dynamics and reversibility of oxygen doping and de-doping for conjugated polymer, *J. Appl. Phys.*, 2008, **103**, 104506.

18 J. A. Merlo, C. R. Newman, C. P. Gerlach, T. W. Kelley, D. V. Muyres, S. E. Fritz, M. F. Toney and C. D. Frisbie, p-Channel Organic Semiconductors Based on Hybrid Acene–Thiophene Molecules for Thin-Film Transistor Applications, *J. Am. Chem. Soc.*, 2005, **127**, 3997–4009.

19 C. Pannemann, T. Diekmann and U. Hilleringmann, Degradation of organic field-effect transistors made of pentacene, *J. Mater. Res.*, 2004, **19**, 1999–2002.

20 K. Takimiya, T. Yamamoto, H. Ebata and T. Izawa, Design strategy for air-stable organic semiconductors applicable to high-performance field-effect transistors, *Sci. Technol. Adv. Mater.*, 2007, **8**, 273–276.

21 T. Yamamoto and K. Takimiya, Facile Synthesis of Highly π-Extended Heteroarenes, Dinaphtho[2,3-b:2′,3′-f]chalcogenopheno[3,2-b]chalcogenophenes, and Their Application to Field-Effect Transistors, *J. Am. Chem. Soc.*, 2007, **129**, 2224–2225.

22 K. Takimiya, I. Osaka, T. Mori and M. Nakano, Organic Semiconductors Based on [1]Benzothieno[3,2-b][1]benzothiophene Substructure, *Acc. Chem. Res.*, 2014, **47**, 1493–1502.

23 M. Kaltenbrunner, T. Sekitani, J. Reeder, T. Yokota, K. Kuribara, T. Tokuhara, M. Drack, R. Schwödiauer, I. Graz, S. Bauer-Gogonea, S. Bauer and T. Someya, An ultra-lightweight design for imperceptible plastic electronics, *Nature*, 2013, **499**, 458–463.

24 S. Lee, A. Reuveny, J. Reeder, S. Lee, H. Jin, Q. Liu, T. Yokota, T. Sekitani, T. Isoyama, Y. Abe, Z. Suo and T. Someya, A transparent bending-insensitive pressure sensor, *Nat. Nanotechnol.*, 2016, **11**, 472–478.

25 T. Sekitani, T. Yokota, K. Kuribara, M. Kaltenbrunner, T. Fukushima, Y. Inoue, M. Sekino, T. Isoyama, Y. Abe, H. Onodera and T. Someya, Ultraflexible organic amplifier with biocompatible gel electrodes, *Nat. Commun.*, 2016, **7**, 11425.

26 M. Sugiyama, T. Uemura, M. Kondo, M. Akiyama, N. Namba, S. Yoshimoto, Y. Noda, T. Araki and T. Sekitani, An ultraflexible organic differential amplifier for recording electrocardiograms, *Nat. Electron.*, 2019, **2**, 351–360.

27 K. Kawabata, S. Usui and K. Takimiya, Synthesis of Soluble Dinaphtho[2,3-b:2′,3′-f]thieno[3,2-b]thiophene (DNTT) Derivatives: One-Step Functionalization of 2-Bromo-DNTT, *J. Org. Chem.*, 2020, **85**, 195–206.

28 K. Takimiya, S. Usui, A. Sato, K. Kanazawa and K. Kawabata, Packing structures of (trialkylsilyl)ethynyl-substituted dinaphtho[2,3-b:2′,3′-f]thieno[3,2-b]thiophenes (DNTTs): effects of substituents on crystal structures and transport properties, *J. Mater. Chem. C*, 2022, **10**, 2775–2782.

29 K. Sumitomo, Y. Sudo, K. Kanazawa, K. Kawabata and K. Takimiya, Enantiopure 2-(2-ethylhexyl)dinaphtho[2,3-b:2′,3′-f]thieno[3,2-b]thiophenes: synthesis, single-crystal structure and a surprising lack of influence of stereoisomerism on thin-film structure and electronic properties, *Mater. Horiz.*, 2022, **9**, 444–451.

30 G. Sheldrick, SHELXT – Integrated space-group and crystal-structure determination, *Acta Crystallogr., Sect. A:Found. Adv.*, 2015, **71**, 3–8.

31 G. Sheldrick, Crystal structure refinement with SHELXL, *Acta Crystallogr., Sect. C:Struct. Chem.*, 2015, **71**, 3–8.

32 O. V. Dolomanov, L. J. Bourhis, R. J. Gildea, J. A. K. Howard and H. Puschmann, OLEX2: a complete structure solution, refinement and analysis program, *J. Appl. Crystallogr.*, 2009, **42**, 339–341.

33 M. J. Frisch, G. W. Trucks, H. B. Schlegel, G. E. Scuseria, M. A. Robb, J. R. Cheeseman, G. Scalmani, V. Barone, G. A. Petersson, H. Nakatsuji, X. Li, M. Caricato, A. V. Marenich, J. Bloino, B. G. Janesko, R. Gomperts, B. Mennucci, H. P. Hratchian, J. V. Ortiz, A. F. Izmaylov, J. L. Sonnenberg, D. Williams-Young, F. Ding, F. Lipparini, F. Egidi, J. Goings, B. Peng, A. Petrone, T. Henderson,

D. Ranasinghe, V. G. Zakrzewski, J. Gao, N. Rega, G. Zheng, W. Liang, M. Hada, M. Ehara, K. Toyota, R. Fukuda, J. Hasegawa, M. Ishida, T. Nakajima, Y. Honda, O. Kitao, H. Nakai, T. Vreven, K. Throssell, J. A. Montgomery Jr., J. E. Peralta, F. Ogliaro, M. J. Bearpark, J. J. Heyd, E. N. Brothers, K. N. Kudin, V. N. Staroverov, T. A. Keith, R. Kobayashi, J. Normand, K. Raghavachari, A. P. Rendell, J. C. Burant, S. S. Iyengar, J. Tomasi, M. Cossi, J. M. Millam, M. Klene, C. Adamo, R. Cammi, J. W. Ochterski, R. L. Martin, K. Morokuma, O. Farkas, J. B. Foresman and D. J. Fox, *Gaussian 16 Rev. C.01.*, 2016.

34 ADF: powerful DFT code for modeling molecules; Scien-tific Computing and Modeling: Amsterdam; https://www.scm.com/ADF/).

35 B. Jeziorski, R. Moszynski and K. Szalewicz, Perturbation Theory Approach to Intermolecular Potential Energy Surfaces of van der Waals Complexes, *Chem. Rev.*, 1994, **94**, 1887–1930.

36 R. M. Parrish, L. A. Burns, D. G. A. Smith, A. C. Simmonett, A. E. DePrince, E. G. Hohenstein, U. Bozkaya, A. Y. Sokolov, R. Di Remigio, R. M. Richard, J. F. Gonthier, A. M. James, H. R. McAlexander, A. Kumar, M. Saitow, X. Wang, B. P. Pritchard, P. Verma, H. F. Schaefer, K. Patkowski, R. A. King, E. F. Valeev, F. A. Evangelista, J. M. Turney, T. D. Crawford and C. D. Sherrill, Psi4 1.1: An Open-Source Electronic Structure Program Emphasizing Automation, Advanced Libraries, and Interoperability, *J. Chem. Theory Comput.*, 2017, **13**, 3185–3197.

37 R. Dovesi, A. Erba, R. Orlando, C. M. Zicovich-Wilson, B. Civalleri, L. Maschio, M. Rérat, S. Casassa, J. Baima, S. Salustro and B. Kirtman, Quantum-mechanical con-densed matter simulations with CRYSTAL, *Wiley Interdiscip. Rev.:Comput. Mol. Sci.*, 2018, **8**, e1360.

38 T. Ishiyama, M. Murata and N. Miyaura, Palladium(0)-Catalyzed Cross-Coupling Reaction of Alkoxydiboron with Haloarenes: A Direct Procedure for Arylboronic Esters, *J. Org. Chem.*, 1995, **60**, 7508–7510.

39 K. Kobashi, R. Hayakawa, T. Chikyow and Y. Wakayama, Negative Differential Resistance Transistor with Organic p-n Heterojunction, *Adv. Electron. Mater.*, 2017, **3**, 1700106.

40 C. Lee, J. Choi, H. Park, C. Lee, C.-H. Kim, H. Yoo and S. G. Im, Systematic Control of Negative Transconductance in Organic Heterojunction Transistor for High-Performance, Low-Power Flexible Ternary Logic Circuits, *Small*, 2021, **17**, 2103365.

41 S. Kim, Y. Jeon, H. R. Cho, C. H. Kim and H. Yoo, Organic Ternary Logic Inverter Using Negative Transconductance Pull-Down Switching Transistor, *IEEE Electron Device Lett.*, 2024, **45**, 590–592.

42 H. Matsui, D. Kumaki, E. Takahashi, K. Takimiya, S. Tokito and T. Hasegawa, Correlation between interdomain carrier hopping and apparent mobility in polycrystalline organic transistors as investigated by electron spin resonance, *Phys. Rev. B:Condens. Matter Mater. Phys.*, 2012, **85**, 035308.

43 Y. Kinoshita, H. Tanaka, Y. Shimoi, K. Takimiya and S.-I. Kuroda, Low-temperature carrier dynamics in high-mobility organic transistors of alkylated dinaphtho-thienothiophene as investigated by electron spin resonance, *Appl. Phys. Lett.*, 2014, **105**, 033301.

44 C. Tanase, E. J. Meijer, P. W. M. Blom and D. M. de Leeuw, Unification of the Hole Transport in Polymeric Field-Effect Transistors and Light-Emitting Diodes, *Phys. Rev. Lett.*, 2003, **91**, 216601.

45 C. G. Shuttle, R. Hamilton, J. Nelson, B. C. O'Regan and J. R. Durrant, Measurement of Charge-Density Dependence of Carrier Mobility in an Organic Semiconductor Blend, *Adv. Funct. Mater.*, 2010, **20**, 698–702.

46 M. Koopmans, M. A. T. Leiviskä, J. Liu, J. Dong, L. Qiu, J. C. Hummelen, G. Portale, M. C. Heiber and L. J. A. Koster, Electrical Conductivity of Doped Organic Semiconductors Limited by Carrier–Carrier Interactions, *ACS Appl. Mater. Interfaces*, 2020, **12**, 56222–56230.

47 R. Takeuchi, S. Izawa, Y. Hasegawa, R. Tsuruta, T. Yamaguchi, M. Meissner, S.-I. Ideta, K. Tanaka, S. Kera, M. Hiramoto and Y. Nakayama, Experimental Observation of Anisotropic Valence Band Dispersion in Dinaphtho[2,3-*b*:2′,3′-*f*]thieno[3,2-*b*]thiophene (DNTT) Single Crystals, *J. Phys. Chem. C*, 2021, **125**, 2938–2943.

48 H. Yagi, T. Miyazaki, Y. Tokumoto, Y. Aoki, M. Zenki, T. Zaima, S. Okita, T. Yamamoto, E. Miyazaki, K. Takimiya and S. Hino, Ultraviolet photoelectron spectra of 2,7-diphenyl[1]benzothieno[3,2-*b*][1]benzothiophene and dinaphtho[2,3-*b*:2′,3′-*f*]thieno[3,2-*b*]thiophene, *Chem. Phys. Lett.*, 2013, **563**, 55–57.

49 I. Salzmann, S. Duhm, G. Heimel, M. Oehzelt, R. Kniprath, R. L. Johnson, J. P. Rabe and N. Koch, Tuning the Ionization Energy of Organic Semiconductor Films: The Role of Intra-molecular Polar Bonds, *J. Am. Chem. Soc.*, 2008, **130**, 12870–12871.

50 G. Heimel, I. Salzmann, S. Duhm and N. Koch, Design of Organic Semiconductors from Molecular Electrostatics, *Chem. Mater.*, 2011, **23**, 359–377.

51 F. Zu, D. Shin and N. Koch, Electronic properties of metal halide perovskites and their interfaces: the basics, *Mater. Horiz.*, 2022, **9**, 17–24.

52 P. M. Kazmaier and R. Hoffmann, A Theoretical Study of Crystallochromy. Quantum Interference Effects in the Spectra of Perylene Pigments, *J. Am. Chem. Soc.*, 1994, **116**, 9684–9691.

53 (*a*) CCDC 2372480: Experimental Crystal Structure Determi-nation, 2026, DOI: 10.5517/ccdc.csd.cc2kmrml; (*b*) CCDC 2519941: Experimental Crystal Structure Determination, 2026, DOI: 10.5517/ccdc.csd.cc2ql6fz.